To appear in ApJ Letters
Preprint typeset using LaTeX style emulateapj v. 5/2/11

arXiv:1402.6755v1 [astro-ph.HE] 27 Feb 2014

X-RAY SPECTRAL COMPONENTS OBSERVED IN THE AFTERGLOW OF GRB 130925A

Eric C. Bellm[1], Nicolas M. Barrière[2], Varun Bhalerao[3], Steven E. Boggs[2], S. Bradley Cenko[4], Finn E. Christensen[5], William W. Craig[2,6], Karl Forster[1], Chris L. Fryer[7], Charles J. Hailey[8], Fiona A. Harrison[1], Assaf Horesh[9], Chryssa Kouveliotou[10], Kristin K. Madsen[1], Jon M. Miller[11], Eran O. Ofek[9], Daniel A. Perley[1], Vikram R. Rana[1], Stephen P. Reynolds[12], Daniel Stern[13], John A. Tomsick[2], and William W. Zhang[4]

To appear in ApJ Letters

ABSTRACT

We have identified spectral features in the late-time X-ray afterglow of the unusually long, slow-decaying GRB 130925A using *NuSTAR*, *Swift*-XRT, and *Chandra*. A spectral component in addition to an absorbed power-law is required at $> 4\sigma$ significance, and its spectral shape varies between two observation epochs at 2×10^5 and 10^6 seconds after the burst. Several models can fit this additional component, each with very different physical implications. A broad, resolved Gaussian absorption feature of several keV width improves the fit, but it is poorly constrained in the second epoch. An additive black body or second power-law component provide better fits. Both are challenging to interpret: the blackbody radius is near the scale of a compact remnant (10^8 cm), while the second powerlaw component requires an unobserved high-energy cutoff in order to be consistent with the non-detection by *Fermi*-LAT.

Subject headings: gamma-ray burst: individual (GRB130925A)

1. INTRODUCTION

Recent work has identified several "ultra-long" gamma-ray bursts (GRBs) with properties distinct from normal long GRBs (Levan et al. 2013, and references therein). These events have initial bursting phases lasting thousands of seconds in gamma-rays and show long-lived, highly variable X-ray afterglows. It is currently unclear whether these bursts are simply extreme examples of the long GRB class, as suggested by Zhang et al. (2013); if they are related to the even longer candidate relativistic Tidal Disruption Events (TDEs) *Swift* J1644+57 (Bloom et al. 2011; Levan et al. 2011; Burrows et al. 2011) and *Swift* J2058+05 (Cenko et al. 2012); or if they represent a new subclass of transient, perhaps with large-radius progenitors (Woosley & Heger 2012; Gendre et al. 2013; Nakauchi et al. 2013).

The bright, nearby GRB 130925A is similar to previously reported ultra-long GRBs and, with the launch of *NuSTAR*, provides an opportunity to observe the X-ray spectrum at high sensitivity over a broad energy band. Here we report time-varying spectral features in the late-time X-ray afterglow of GRB 130925A that were initially discovered by *NuSTAR* and confirmed in a second epoch by *NuSTAR* and *Chandra*. Our detections are at higher energies and significantly later times than previously reported afterglow features.

Before the era of routine afterglow observations with *Swift*-XRT, several authors claimed detection of lines in GRB X-ray afterglows on top of otherwise smooth power-law spectra (e.g., Piro et al. 2000; Amati et al. 2000; Reeves et al. 2002). Most reports were of emission lines at relatively low signal-to-noise ratio, and there was substantial controversy over the methods used to assess line significance (Protassov et al. 2002; Sako et al. 2005). Since the advent of *Swift*, no firm afterglow line detections have been reported despite its greater sensitivity and systematic followup, calling previous reports into question (for a review, see Hurkett et al. 2008).

However, statistically significant blackbody components have been reported in the early-time ($t \lesssim 10^3$ s) afterglow spectra of several bursts observed by *Swift*-XRT (Starling et al. 2012, and references therein). The inferred rest-frame temperatures are typically a few tenths of a keV, the inferred radii are $\sim 10^{12}$ cm, and the blackbody component provides 10–50% of the 0.3–10 keV flux. The first detections were in low-luminosity, SN-associated GRBs, leading to suggestions that the emission was due to shock breakout from the SN (e.g., Campana et al. 2006). Systematic searches have found thermal components in early afterglows of classical GRBs as well (Sparre & Starling 2012; Friis & Watson 2013), giving credence to alternative interpretations including late-time emission from a prompt photosphere (Friis & Watson 2013) or emission from a cocoon around the jet (Suzuki & Shigeyama 2013; Nakauchi et al. 2013).

Of particular relevance are reports of additional com-

[1] Cahill Center for Astronomy and Astrophysics, California Institute of Technology, Pasadena, CA 91125; ebellm@caltech.edu.
[2] Space Sciences Laboratory, University of California, Berkeley, CA 94720
[3] Inter-University Center for Astronomy and Astrophysics, Post Bag 4, Ganeshkhind, Pune 411007, India
[4] NASA Goddard Space Flight Center, Greenbelt, MD 20771
[5] DTU Space - National Space Institute, Technical University of Denmark, Elektrovej 327, 2800 Lyngby, Denmark
[6] Lawrence Livermore National Laboratory, Livermore, CA 94550
[7] CCS-2, Los Alamos National Laboratory, Los Alamos, NM 87545
[8] Columbia Astrophysics Laboratory, Columbia University, New York, NY 10027
[9] Benoziyo Center for Astrophysics, Weizmann Institute of Science, 76100 Rehovot, Israel.
[10] Astrophysics Office/ZP12, NASA Marshall Space Flight Center, Huntsville, AL 35812, USA
[11] Department of Astronomy, The University of Michigan, 500 Church Street, Ann Arbor, MI, 48109
[12] Physics Dept., NC State U., Raleigh, NC 27695
[13] Jet Propulsion Laboratory, California Institute of Technology, Pasadena, CA 91109

ponents in the afterglows of other ultra-long GRBs. The "Christmas Day Burst" GRB 101225A showed evidence of two separate blackbody components, a 1 keV X-ray black body with radius 2×10^{11} cm observed 6 ksec after the burst and a UVOIR black body with radius $2–7 \times 10^{14}$ cm which cooled over 18 days (Thöne et al. 2011). In GRB 111209A, Stratta et al. (2013) reported the *XMM* detection of a second, hard power-law component ($\Gamma \sim 0$) during the steep decay phase ~70 ksec after the burst.

2. OBSERVATIONS

GRB 130925A produced several emission episodes triggering *Swift*-BAT, *Fermi*-GBM, and *MAXI*. *Swift*-BAT triggered on GRB 130925A at T_0 = 2013-09-25 04:11:24 UT (Lien et al. 2013). *Fermi* GBM triggered on a precursor episode about 15 minutes before the *Swift* trigger (Fitzpatrick & the Fermi GBM Team 2013), and *MAXI* triggered on an emission episode nearly 4 ksec after the initial *Swift* trigger (Suzuki et al. 2013). The final BAT detection of the emission occurred during a flare observed by XRT, at $T_0 + 7.1$ ksec (Markwardt et al. 2013). Despite an automated repointing, *Fermi*-LAT did not detect any emission (Kocevski et al. 2013). Both the *INTEGRAL*-SPI Anti-Coincidence Shield and *Konus-WIND* detected gamma-rays from the burst over a total interval of nearly 5 ksec (Savchenko et al. 2013; Golenetskii et al. 2013).

Swift-XRT observed large, repeated flares from the burst (Evans et al. 2013; Figure 1). The extraordinary length of the bursting phase led Burrows et al. (2013) to suggest similarity to the proposed jetted TDE *Swift* J1644+57, although Golenetskii et al. (2013) argued that some previous ultra-long events thought to be GRBs had been observed with similar total duration.

Starting around 2×10^4 sec after the *Swift* trigger, the X-ray afterglow entered a steady decay phase without new flares (Figure 1). The observed decline is similar to other GRB afterglows and differs markedly from the weeks of flaring observed for *Swift* J1644+57.

In contrast, the source was faint at optical–NIR wavelengths. Rapid followup observations found a NIR-bright ($K = 18$, $r' > 22$ mag AB) source near the X-ray position (Sudilovsky et al. 2013a). Spectroscopy of the host galaxy provided a redshift of $z = 0.347$ (Vreeswijk et al. 2013; Sudilovsky et al. 2013b). Late-time *HST* imaging showed that the event took place in the plane of a disrupted host galaxy but offset 0.12 arcsec (600 pc in projection) from the galaxy nucleus (Tanvir et al. 2013). This offset disfavors a TDE origin for this event, although the authors noted that a galaxy merger could produce a supermassive black hole offset from the light centroid.

NuSTAR (Harrison et al. 2013) provides unprecedented X-ray sensitivity above 10 keV thanks to the combination of its multilayer-coated focusing optics and CdZnTe detectors. *NuSTAR* observed GRB 130925A during the decay phase beginning 1.8 days after the *Swift* trigger (Figure 1). The total on-source observation time in the first epoch was 39.2 ksec. Our initial analysis showed that an absorption feature was needed to fit the *NuSTAR* data (Bellm et al. 2013). We triggered two additional *NuSTAR* observations of 88.2 and 90.7 ksec integration time; these occurred at 8.8 and 11.3 days after the *Swift* trigger. We also obtained a 44.3 ksec

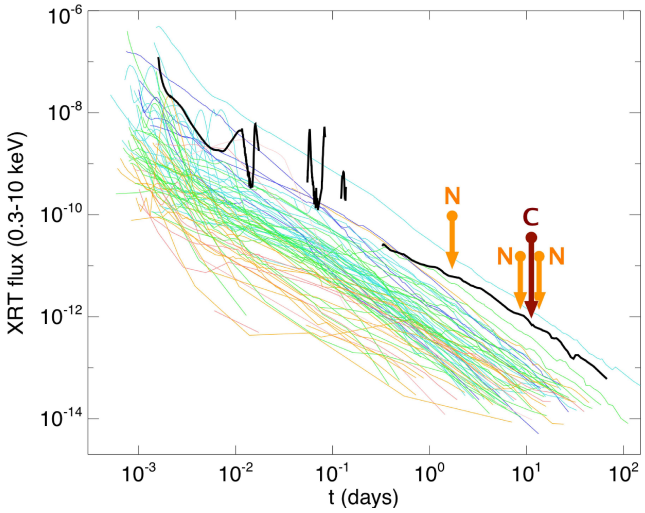

Figure 1. *Swift*-XRT lightcurve for GRB 130925A (black) plotted over the XRT lightcurves of other afterglows. The *NuSTAR* (N) and *Chandra* (C) observation times are marked.

Director's Discretionary Time observation with *Chandra* ACIS-S beginning 11.0 days after the *Swift* trigger.

3. DATA REDUCTION

We processed the *NuSTAR* data with HEASOFT 6.14 and the *NuSTAR* Data Analysis Software (NuSTARDAS) v.1.2.0 using CALDB version 20130509. We extracted source counts from circular regions with 40 arcsec radius from both *NuSTAR* modules. We identified background regions of 125 arcsec radius on the same *NuSTAR* detectors as the source. Since the second and third *NuSTAR* observations and the *Chandra* observation are nearly contiguous in time and the source is only slowly varying, we analyzed these data together and refer to them hereafter as the second epoch. We combined the *NuSTAR* data from the second and third observations and from both modules into a single spectrum to maximize the signal-to-noise ratio.

We also downloaded and reduced the 13.0 ksec of *Swift*-XRT PC-mode data contemporaneous with the first *NuSTAR* epoch (`obsid 00571830006`) using standard procedures in HEASOFT 6.14.

We processed the *Chandra* data using standard procedures with CIAO v4.5. The data were obtained using 1/4 Window readout to reduce pileup; we verified that the effect of pileup on our spectra is negligible and ignore it in further analysis.

We rebinned all of the data to > 20 counts per bin and fit the data using ISIS v1.6.2-19. We also required the *NuSTAR* bins to have SNR of > 4.5, as above ~ 15 keV the background dominates. We minimized χ^2 in our fits to the data and use the covariance matrix in our significance calculations in Section 4. We used fit energy bands of 3–30 keV (*NuSTAR*), 0.3–10 keV (*Swift*-XRT), and 0.2–10 keV (*Chandra*). All errors are 90% C.L., and we have used a cosmology with $h = 0.704$, $\Omega_M = 0.273$, $\Omega_\Lambda = 0.727$ (Komatsu et al. 2011).

4. SPECTRAL MODELING

4.1. *Single Power law*

GRB X-ray afterglow spectra are usually well-fit by absorbed power law (PL) models. We froze a Galactic

$N_{\rm H}$ component of $1.7 \times 10^{20}\,{\rm cm}^{-2}$ (Kalberla et al. 2005; Evans et al. 2013) and allowed a varying $N_{\rm H}$ component at the reported redshift of $z = 0.347$.

A PL fit to the first epoch *NuSTAR* data shows a clear deficit in the residuals in the 5–6 keV region (Figure 2). A joint PL fit including the *Swift*-XRT data improves the parameter constraints, particularly for $N_{\rm H}$, but the residual structure remains. The goodness of fit is poor, with $\chi^2_\nu = 1.6$ (Table 1). A PL fit to the *Chandra* data and a joint *NuSTAR*-*Chandra* PL fit also show residual structure (Figure 3) and poor goodness of fit, with $\chi^2_\nu = 2.2$. Additional components (Sections 4.2–4.5) improve these fits.

4.2. *Absorption Feature*

Multiplying by a Gaussian absorber (`gabs`×PL) in the first epoch markedly improves the fit residuals relative to a PL fit (Figure 2). The centroid of the Gaussian absorber is at $5.9^{+0.4}_{-0.3}\,{\rm keV}$, and $\sigma = 0.9^{+0.6}_{-0.3}\,{\rm keV}$, both in the observer frame. The *Swift* data show similar residual structure, and in a joint fit the Gaussian absorber gives a similar centroid ($6.0^{+0.5}_{-0.3}\,{\rm keV}$) but greater width ($1.8^{+1.9}_{-0.7}\,{\rm keV}$; Table 1). In the joint fit, χ^2_ν improves to 1.1 from 1.6 for three additional parameters.

In the second epoch, a Gaussian absorber again improves the fit relative to a PL ($\chi^2_\nu = 1.2$ from 2.2), but the parameters are poorly constrained. The joint *NuSTAR* and *Chandra* fit provides only an upper limit (4.1 keV) on the line centroid. This value is inconsistent with that of the first epoch, and the required line width is substantially larger ($\sigma = 5.2^{+2.0}_{-3.0}\,{\rm keV}$, Figure 4). The large shift in the line centroid is difficult to explain with absorption by a single species. If the large linewidth is interpreted as turbulent velocity broadening, this implies relativistic velocities $\gtrsim 0.1c$ that increase from the first epoch to the second, an unlikely scenario.

4.3. *Bremsstrahlung*

We obtained good fits ($\chi^2_\nu \sim 1.1$) with an absorbed bremsstrahlung plus power-law model (Bremss+PL). The component is well-constrained in both epochs, with best-fit temperatures of 1.3±0.2 and $0.83^{+0.12}_{-0.11}\,{\rm keV}$ in the comoving frame. The fit emission measures are $1.1^{+0.5}_{-0.3}\times10^{69}\,{\rm cm}^{-3}$ and $2.3^{+0.9}_{-0.6}\times10^{68}\,{\rm cm}^{-3}$. These extreme emission measures, if produced by a constant-density medium, would require densities of order $10^{10}(R/10^{16}\,{\rm cm})^{-3/2}\ {\rm cm}^{-3}$. However, a circumstellar medium this dense would be optically thick to electron scattering, violating the assumptions of the optically thin bremsstrahlung model. The emitting region would be optically thin only if the radius of the region were $> 10^{20}\,{\rm cm}$, much larger than typical afterglow radii. More complex density profiles would require even higher densities at some locations. Thus while the addition of an optically thin bremsstrahlung spectral component improves the fit to the data, we are unable to construct a self-consistent physical interpretation for it. This problem persists even if instead we require a higher temperature for the bremsstrahlung component in order to fit the high-energy excess. The fit is worse (χ^2 increases by 5.9 in both epochs) and provides only a lower limit on the temperature ($kT \gtrsim 25\,{\rm keV}$ in the comoving frame).

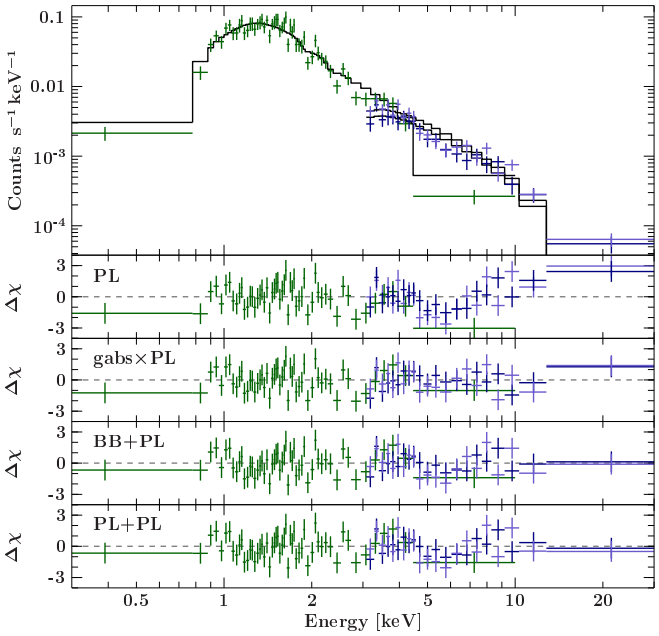

Figure 2. Spectral fits to the first epoch *NuSTAR* and *Swift* data. The top panel shows the count spectra and PL model fit. The lower panels show the residuals for the PL, `gabs`×PL, BB+PL, and PL+PL fits. Data are colored blue (*NuSTAR* module A), navy blue (module B) and green (*Swift*-XRT).

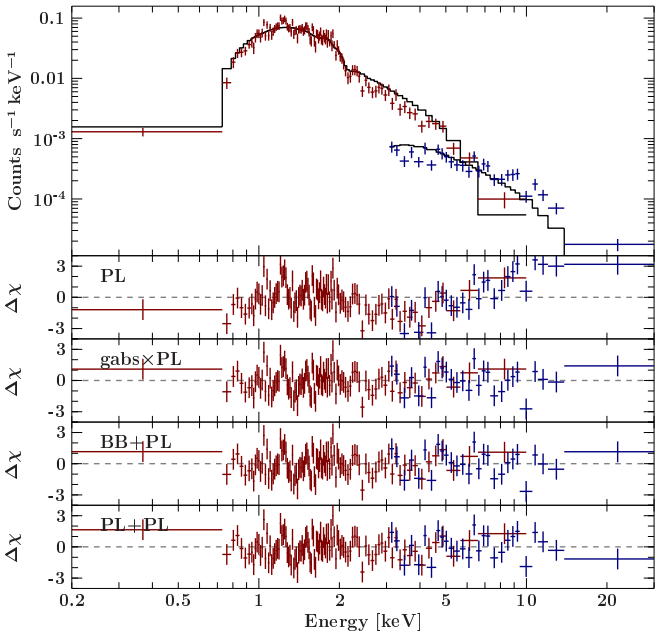

Figure 3. Spectral fits to the second epoch *NuSTAR* and *Chandra* data. Panels are as in Figure 2. The *Chandra* data are red, and data from the combined *NuSTAR* modules are navy blue.

The emission region must still be larger than $10^{18}\,{\rm cm}$ to be optically thin.

Motivated by the presence of possible additional residual structure in the *Chandra* data in the 1–3 keV range, we attempted to fit `mekal` and `apec` plasma emission models to the second-epoch data. With standard abundances, these models fit metallicity values of zero, reproducing the unphysical Bremss+PL model. Even with highly variable abundances, single-temperature plasmas did not provide clear improvements in the fit.

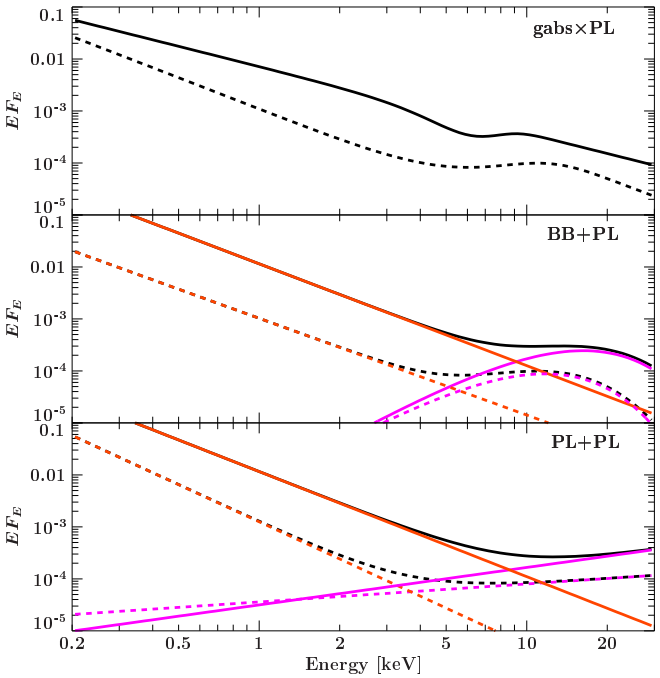

Figure 4. Unfolded, unabsorbed model spectra for the gabs×PL, BB+PL, and PL+PL fits in $\mathrm{keV^2\,cm^{-2}\,s^{-1}\,keV^{-1}}$. Fits to the first (second) epoch are plotted with solid (dashed) lines. For the BB+PL and PL+PL fits, the total model is plotted in black, the power law component in orange, and the black body or second power law component in pink.

4.4. *Black Body*

We also fit a black body plus power-law model (BB+PL). The χ^2 surface shows two minima for the blackbody temperature in both epochs, one near 5 keV and the second near 0.5 keV. In the first epoch the higher temperature is preferred ($\chi^2_{\rm low} = 115.3$ vs. $\chi^2_{\rm high} = 103.1$ for 90 d.o.f.), while in the second epoch the goodness of fit is closer to equivalent ($\chi^2_{\rm low} = 156.2$ vs. $\chi^2_{\rm high} = 157.7$ for 130 d.o.f). We argue that the higher-temperature black body fit is more plausible due to its relative consistency with the component observed in the first epoch and with theoretical expectations (Section 5).

The blackbody components provide 11% (29%) of the total 0.3–30 keV flux in the first (second) epoch. The implied radii for a spherical emission region are small and consistent with constant size: $1.1^{+0.5}_{-0.8} \times 10^8$ cm and $1.5^{+0.5}_{-0.6} \times 10^8$ cm. (The radii for the disfavored low-temperature black bodies are larger but also relatively compact. However, they imply a physically unlikely *contraction* of the emitting region from $(3.2 \pm 0.8) \times 10^{10}$ cm to $(1.7 \pm 0.4) \times 10^{10}$ cm.)

While black body components have been reported in other GRB afterglow spectra, none have been observed at such late times, with such high temperatures, or with such small radii. At 1–10 days after the burst, the blackbody radius inferred from GRB 101225A was over 10^{14} cm and could be explained by the jet interaction with the circumstellar medium (Thöne et al. 2011). The inferred radius of 10^8 cm for GRB 130925A is much harder to explain with a jet interaction model. This size scale is instead on par with the radius of the fallback accretion disks expected in stellar collapse (Fryer 2009).

If we assume we are observing this disk, the fit temperature can place constraints on the progenitor by constraining the conditions in the disk. The luminosity of an accretion disk is roughly equal to the potential energy released in the accretion. If we consider material at radius r, the luminosity (L) is given by $L = GM_{\rm BH}\dot{m}dr/r^2$ where $\dot{m}$ is the accretion rate and dr denotes a small annulus of material at radius r (integrating over dr would produce the total luminosity). The blackbody emission for such an annulus is $L = \sigma AT^4 = \sigma 2\pi r dr$, where σ is the Stefan-Boltzmann constant and T is the blackbody temperature. If we know the temperature, we can then derive the accretion rate $\dot{m} = (2\pi r^3 \sigma T^4)/(GM_{\rm BH})$. For our observed temperatures of 4-5.6 keV, the corresponding accretion rate is $10^{-9} - 10^{-10} \mathrm{M_\odot s^{-1}}$. Fallback $10^5 - 10^6$ s after a supernova or GRB explosion has been calculated for a range of progenitors and explosion energies (MacFadyen et al. 2001; Wong et al. 2014). Fallback at late times follows a simple power law (Chevalier 1989) and depends on the progenitor and the explosion energy of the supernova associated with the GRB. Most fallback calculations (MacFadyen et al. 2001; Wong et al. 2014) predict fallback rates of $10^{-7} - 10^{-10} \mathrm{M_\odot s^{-1}}$ at $10^5 - 10^6$ s for supernova explosions of $1 - 3 \times 10^{51}$ erg.

Our accretion rates imply a luminosity near 10^5 times the Eddington limit for a stellar mass black hole. Although such extreme super-Eddington emission rates have been invoked from fallback (Dexter & Kasen 2013), the exact nature of such transient accretion is not well known. Steady-state solutions of disk accretion find that maintaining emission rates even an order of magnitude above Eddington is difficult (Jaroszynski et al. 1980). Whether such steady state limits apply in transient situations like our fallback disk remains to be seen (Abramowicz 2005). Thus without a full model of these transient events, we are not able to establish a self-consistent explanation for the blackbody emission.

4.5. *Hard Power Law*

Finally, we considered a two power law model (PL+PL) like that reported for GRB 111209A (Stratta et al. 2013). This model is a slightly worse fit in both epochs than the BB+PL model for the same number of free parameters (Table 1).

Stratta et al. (2013) interpret the very hard ($\Gamma \sim 0$) second PL component they report for GRB 111209A at 70 ksec after the burst as the tail of the hard power-law emission sometimes observed by *Fermi*-LAT (e.g., Zhang et al. 2011, and references therein). This component is detected in the late prompt and early afterglow phases and decays according to a power-law; its physical origin remains uncertain. The non-detection by LAT of both GRBs complicates this interpretation. An extrapolation of our Epoch 1 powerlaw flux to the 0.1–10 GeV band gives a photon flux of 3×10^{-6} photons $\mathrm{cm^{-2}\,s^{-1}}$, a value higher than the upper limit of 7×10^{-7} photons $\mathrm{cm^{-2}\,s^{-1}}$ reported by Kocevski et al. (2013) in the first 2 ksec after the burst, when the afterglow—and thus presumably the hard component—was much brighter. The problem is even more severe for the component reported by Stratta et al. (2013): its higher flux and much harder spectral index extrapolate to a 0.1–10 GeV photon flux of

1.5 photons $\mathrm{cm}^{-2}\,\mathrm{s}^{-1}$, an extremely high value sufficient to trigger LAT. We examined the late-time LAT data for both bursts and confirm no excess emission. Consistency with the nondetection by LAT in both cases thus requires a cutoff above the *NuSTAR* and *XMM* bandpasses but below the the LAT bandpass at 30 MeV. This phenomenological model is plausible, but the connection of these components to the early-time hard power-law components detected by LAT in other GRBs therefore remains speculative.

4.6. *Component significance*

We verified the significance of the additional spectral components using Monte Carlo simulations according to the method of posterior predictive p-values (ppp-values; Protassov et al. 2002). We initialized each fit by stepping the additional feature through a grid in energy and finding the largest relative improvement in χ^2 (c.f. Hurkett et al. 2008). This procedure accounts for the "look-elsewhere" effect of multiple trials, as we have no *a priori* expectation of the observed line energy or component temperature. In none of our 10^4 simulated realizations of a null PL model did fits with alternative models (`gabs`×PL, BB+PL, or PL+PL) produce improvements in χ^2 as large as observed in the real data. This implies that the spectral features are significant at $> 3.9\sigma$ in both epochs: the χ^2 improvement for each model fit is extremely unlikely to be due to chance if the true underlying model were simply an absorbed PL.

5. CONCLUSION

Our late-time afterglow observations of GRB 130925A require an additional spectral component at high significance. Several alternative models provide acceptable fits to the data. These spectral features are detected more than 1 Msec after the burst, much later than any components previously reported in X-ray afterglows, probing a largely unexplored phase of afterglow evolution. Several unique features of GRB 130925A make it possible to detect these late-time features for the first time. The unusually bright afterglow enables high-quality spectral fits, and *NuSTAR* has excellent sensitivity at the relevant energies and can constrain the continuum above 10 keV. Moreover, the primary power law is unusually soft, so the high-energy component is not swamped. It is not yet clear whether this emission is related to progenitor physics unique to this unusual, ultra-long burst; *NuSTAR* observations of the bright "canonical" long GRB 130427A were consistent with emission by a single spectral component (Kouveliotou et al. 2013). Future observations of bright afterglows will be needed to determine the prevalence of these late-time spectral components and identify the relevant emission mechanism.

This work was supported under NASA Contract No. NNG08FD60C and uses data from the *NuSTAR* mission, a project led by the California Institute of Technology, managed by the Jet Propulsion Laboratory, and funded by the National Aeronautics and Space Administration. We thank the *NuSTAR* Operations team for executing the ToO observations. This research has used the *NuSTAR* Data Analysis Software (NuSTARDAS) jointly developed by the ASI Science Data Center (ASDC, Italy) and the California Institute of Technology (USA). These results are based in part on observations made by the *Chandra* X-ray Observatory. We thank the *Chandra* director for granting discretionary time and the *Chandra* team for prompt execution of the observations.

Facilities: NuSTAR, Swift, Chandra.

REFERENCES

Abramowicz, M. A. 2005,
in Growing Black Holes: Accretion in a Cosmological Context, ed. A. Merlon 257
Amati, L., Frontera, F., Vietri, M., et al. 2000, Science, 290, 953
Bellm, E. C., Harrison, F. A., Forster, K., et al. 2013, GRB Coordinates Network, 15286, 1
Bloom, J. S., Giannios, D., Metzger, B. D., et al. 2011, Science, 333, 203
Burrows, D. N., Malesani, D., Lien, A. Y., Cenko, S. B., & Gehrels, N. 2013, GRB Coordinates Network, 15253, 1
Burrows, D. N., Kennea, J. A., Ghisellini, G., et al. 2011, Nature, 476, 421
Campana, S., Mangano, V., Blustin, A. J., et al. 2006, Nature, 442, 1008
Cenko, S. B., Krimm, H. A., Horesh, A., et al. 2012, ApJ, 753, 77
Chevalier, R. A. 1989, ApJ, 346, 847
Dexter, J., & Kasen, D. 2013, ApJ, 772, 30
Evans, P. A., Pagani, C., Page, K. L., et al. 2013, GRB Coordinates Network, 15254, 1
Fitzpatrick, G., & the Fermi GBM Team. 2013, GRB Coordinates Network, 15255, 1
Friis, M., & Watson, D. 2013, ApJ, 771, 15
Fryer, C. L. 2009, ApJ, 699, 409
Gendre, B., Stratta, G., Atteia, J. L., et al. 2013, ApJ, 766, 30
Golenetskii, S., Aptekar, R., Frederiks, D., et al. 2013, GRB Coordinates Network, 15260, 1
Harrison, F. A., Craig, W. W., Christensen, F. E., et al. 2013, ApJ, 770, 103
Hurkett, C. P., Vaughan, S., Osborne, J. P., et al. 2008, ApJ, 679, 587
Jaroszynski, M., Abramowicz, M. A., & Paczynski, B. 1980, Acta Astron., 30, 1
Kalberla, P. M. W., Burton, W. B., Hartmann, D., et al. 2005, A&A, 440, 775
Kocevski, D., Racusin, J., Vianello, G., Axelsson, M., & Omodei, N. 2013, GRB Coordinates Network, 15268, 1
Komatsu, E., Smith, K. M., Dunkley, J., et al. 2011, ApJS, 192, 18
Kouveliotou, C., Granot, J., Racusin, J. L., et al. 2013, ApJ, 779, L1
Levan, A. J., Tanvir, N. R., Cenko, S. B., et al. 2011, Science, 333, 199
Levan, A. J., Tanvir, N. R., Starling, R. L. C., et al. 2013, ArXiv e-prints, arXiv:1302.2352 [astro-ph.HE]
Lien, A. Y., Markwardt, C. B., Page, K. L., et al. 2013, GRB Coordinates Network, 15246, 1
MacFadyen, A. I., Woosley, S. E., & Heger, A. 2001, ApJ, 550, 410
Markwardt, C. B., Barthelmy, S. D., Baumgartner, W. H., et al. 2013, GRB Coordinates Network, 15257, 1
Nakauchi, D., Kashiyama, K., Suwa, Y., & Nakamura, T. 2013, ApJ, 778, 67
Piro, L., Garmire, G., Garcia, M., et al. 2000, Science, 290, 955
Protassov, R., van Dyk, D. A., Connors, A., Kashyap, V. L., & Siemiginowska, A. 2002, ApJ, 571, 545
Reeves, J. N., Watson, D., Osborne, J. P., et al. 2002, Nature, 416, 512
Sako, M., Harrison, F. A., & Rutledge, R. E. 2005, ApJ, 623, 973
Savchenko, V., Beckmann, V., Ferrigno, C., et al. 2013, GRB Coordinates Network, 15259, 1
Sparre, M., & Starling, R. L. C. 2012, MNRAS, 427, 2965
Starling, R. L. C., Page, K. L., Pe'Er, A., Beardmore, A. P., & Osborne, J. P. 2012, MNRAS, 427, 2950
Stratta, G., Gendre, B., Atteia, J. L., et al. 2013, ApJ, 779, 66
Sudilovsky, V., Kann, D., Greiner, J., & GROND team. 2013a, GRB Coordinates Network, 15247, 1

Table 1
Best-fit parameters of spectral models. Errors are 90% C.L.

	NuSTAR & *Swift* Epoch 1				*NuSTAR* & *Chandra* Epoch 2			
Parameter	PL	gabs×PL	BB+PL	PL+PL	PL	gabs×PL	BB+PL	PL+PL
$N_{\rm H}$ (10^{22} cm^{-2})	$2.55^{+0.24}_{-0.23}$	$2.71^{+0.41}_{-0.30}$	$3.32^{+0.35}_{-0.34}$	$3.35^{+0.40}_{-0.37}$	1.98±0.14	$2.82^{+0.31}_{-0.439}$	$2.74^{+0.21}_{-0.20}$	$3.02^{+0.29}_{-0.27}$
Γ	3.33±0.13	$3.29^{+0.17}_{-0.14}$	$3.96^{+0.24}_{-0.23}$	$4.02^{+0.33}_{-3.47}$	3.06±0.11	$3.95^{+0.55}_{-0.87}$	$3.86^{+0.20}_{-0.19}$	$4.37^{+0.40}_{-0.12}$
Γ_2				$1.28^{+0.65}_{-0.73}$				$1.65^{+0.26}_{-0.29}$
E_0 (keV)		$5.89^{+0.53}_{-0.33}$				< 4.09		
σ (keV)		$1.75^{+1.97}_{-0.70}$				$5.15^{+1.97}_{-2.97}$		
$\tau(E = E_0)$		$0.73^{+0.12}_{-0.18}$				$2.8^{+1.3}_{-1.8}$		
kT (comoving frame, keV)			$5.58^{+2.12}_{-1.15}$				$4.02^{+0.73}_{-0.56}$	
χ^2/ν	146.8/92	98.1/89	103.1/90	105.9/90	288.8/132	158.9/129	157.7/130	161.0/130
$P_\chi(X > \chi\|\nu)$	2.5E-4	0.23	0.16	0.12	1.0E-13	0.04	0.05	0.03

Sudilovsky, V., Kann, D., Schady, P., et al. 2013b, GRB Coordinates Network, 15250, 1

Suzuki, A., & Shigeyama, T. 2013, ApJ, 764, L12

Suzuki, K., Sakakibara, H., Negoro, H., et al. 2013, GRB Coordinates Network, 15248, 1

Tanvir, N. R., Levan, A. J., Hounsell, R., et al. 2013, GRB Coordinates Network, 15489, 1

Thöne, C. C., de Ugarte Postigo, A., Fryer, C. L., et al. 2011, Nature, 480, 72

Vreeswijk, P. M., Malesani, d., Fynbo, J. P. U., De Cia, A., & Ledoux, C. 2013, GRB Coordinates Network, 15249, 1

Wong, T.-W., Fryer, C. L., Ellinger, C. I., Rockefeller, G., & Kalogera, V. 2014, ArXiv e-prints, arXiv:1401.3032 [astro-ph.HE]

Woosley, S. E., & Heger, A. 2012, ApJ, 752, 32

Zhang, B.-B., Zhang, B., Murase, K., Connaughton, V., & Briggs, M. S. 2013, ArXiv e-prints, arXiv:1310.2540 [astro-ph.HE]

Zhang, B.-B., Zhang, B., Liang, E.-W., et al. 2011, ApJ, 730, 141